hydrogen

MDPI

Article

Kinetic Uncertainty in Hydrogen Jet Flames Using Lagrangian Particle Statistics

Shuzhi Zhang *, Vansh Sharma and Venkat Raman

Department of Aerospace Engineering, University of Michigan, Ann Arbor, MI 48109, USA; vanshs@umich.edu (V.S.); ramanvr@umich.edu (V.R.)
* Correspondence: szzhang@umich.edu; Tel.: +1-734-496-4796

Abstract

Hydrogen-enriched fuel injection in staged gas-turbine combustors is commonly achieved through jet-in-crossflow (JICF) configurations, where flame stabilization is governed by a local balance between flow-induced strain/mixing and chemical reaction rates. This work investigates turbulent reacting JICF relevant to staged combustion conditions using high-fidelity simulations with adaptive mesh refinement (AMR) and differential-diffusion effects together with Lagrangian particle statistics. Chemistry model uncertainties are incorporated by using a projection method that maps uncertainty estimates from detailed mechanisms into the model used in this work. Results show that the macroscopic flame topology remains in a stable two-branch regime (lee-stabilized and lifted) and is primarily controlled by the jet momentum–flux ratio J. Visualization of the normalized scalar dissipation rate reveals that the flame front resides on the low-dissipation side of intense mixing layers, occupying an intermediate region between over-strained and under-mixed regions. While hydrogen content does not significantly change the global stabilization mode for the cases studied, uncertainty analysis reveals composition-dependent differences that are not apparent in the mean behavior alone. In particular, visualization in Eulerian (χ, T) state-space analysis and particle statistics conditioned on the stoichiometric surface demonstrate that higher-hydrogen cases observe a lower scalar dissipation rate and exhibit substantially reduced variability in OH production under kinetic-parameter perturbations, whereas lower-hydrogen blends experience higher dissipation and amplified chemical sensitivity. These findings highlight that, even in globally similar JICF regimes, the hydrogen content can modify the local response of the flame to kinetic-parameter uncertainty, motivating uncertainty-aware interpretation and design for hydrogen-fueled staging systems.

Keywords: jet in crossflow; Lagrangian particles; hydrogen combustion; adaptive mesh refinement; turbulent combustion; reaction sensitivity; uncertainty quantification

Check for updates

Academic Editor: Guo-Ming Weng

Received: 18 March 2026
Revised: 14 April 2026
Accepted: 19 April 2026
Published: 22 April 2026

Copyright: © 2026 by the authors. Licensee MDPI, Basel, Switzerland. This article is an open access article distributed under the terms and conditions of the Creative Commons Attribution (CC BY) license.

1. Introduction

Hydrogen is an attractive energy carrier for low-carbon energy systems because it can be produced from renewable electricity and enables deep de-carbonization pathways across multiple sectors. In near- to mid-term gas-turbine applications, a practical route toward hydrogen utilization is blending hydrogen with a primary fuel such as natural gas to expand operability while reducing carbon intensity [1]. In modern combustors, fuel–air mixing and flame stabilization are frequently achieved via staged injection strategies, for which the canonical jet-in-crossflow (JICF) configuration provides a representative model

problem [2]. In gas turbines, the crossflow may consist of high-pressure, high-temperature compressor air in primary burners [1], or hot products in axial staging configurations [3].

Despite its benefits, hydrogen combustion presents stringent operability constraints because its high reactivity and diffusivity increase susceptibility to flashback, blowout, and other stability-limiting phenomena [4–6]. In reacting JICF, stabilization is governed by a local balance between flow-induced strain/mixing and chemical reaction rates: the crossflow and jet establish shear-layer and recirculation structures that set residence times and local mixing rates, while chemistry must remain fast enough to sustain heat release against strain-driven scalar-gradient dissipation. Consequently, flame morphology and anchoring are strongly conditioned by the strain environment associated with the momentum–flux ratio and the resulting vortical dynamics [2,7]. Hydrogen also introduces thermodiffusive effects (Lewis-number effects) through preferential and differential diffusion, which can shift local composition and displace the reaction zone relative to nominal stoichiometric surfaces, particularly in low-speed, high-residence-time regions; while important, these transport effects are not the primary focus here and are treated as part of the physics captured by the employed transport model [8,9].

Several studies have examined reacting JICF dynamics and flame stabilization with hydrogen-containing fuels. Minamoto et al. [10] investigated stabilization trends under varying compositions and differential diffusion. Nair and co-workers [11,12] showed that flame location can feedback on shear-layer dynamics and vortex structure in reacting JICF. Grout et al. [13] performed DNS of reacting JICF and observed stabilization in low-speed regions, though without isolating Lewis-number effects. Sharma et al. [7] conducted LES with a strain-sensitive flamelet approach and compared it against the experiments of Steinberg et al. [14], capturing multiple flame branches and a lee-stabilized branch anchored to the jet; however, unity-Lewis-number assumptions limited accuracy in predicting flame location under all conditions. Collectively, these works highlight the multi-branch nature of reacting JICF and reinforce that the governing mechanism is the local competition between strain/mixing and chemistry, while hydrogen-specific transport can modulate where the flame resides within the complex JICF flowfield.

Beyond transport and turbulence–chemical interaction, predictive modeling is also limited by uncertainties in chemical kinetics. Reaction-rate parameters carry non-negligible uncertainties that can impact radical production, ignition/extinction propensity, and the sensitivity of key reaction pathways [15–19]. While uncertainty estimates for detailed mechanisms have begun to emerge [20], the forward propagation of correlated kinetic uncertainty through practical CFD remains difficult both because ensemble sampling with detailed chemistry is prohibitively expensive and large-scale simulations commonly rely on reduced mechanisms. Importantly, uncertainty information is rarely available for reduced mechanisms and cannot be transferred trivially from detailed mechanisms: reduction removes pathways, may lump reactions, and can introduce steady-state assumptions, breaking a one-to-one correspondence between parameter sets. This gap motivates uncertainty frameworks that preserve the computational efficiency of reduced-chemistry CFD while recovering mechanism-consistent uncertainty information for reacting-flow quantities of interest.

The present work addresses these coupled challenges—strain-conditioned stabilization in reacting JICF and mechanism-consistent kinetic uncertainty—within staged configurations relevant to gas-turbine fuel injection. High-fidelity simulations with adaptive mesh refinement are performed for operating conditions based on the experiments of Steinberg et al. [14]: selected cases are used for validation against measurements, and an additional higher-hydrogen case is introduced to probe how hydrogen content modulates chemical sensitivity under comparable flow conditions. To capture hydrogen-transport

physics without invoking unity-Lewis-number closures, a mixture-averaged diffusion model is employed. To incorporate kinetic uncertainty at practical cost, a correlated uncertainty model is introduced via a covariance-transfer (and refinement) procedure: the available parameter covariance from the detailed FFCM-2 mechanism [20] is reduced and mapped to a computationally efficient H_2–air mechanism [21], enabling uncertainty quantification and reaction-sensitivity analysis without requiring full-field ensemble CFD with detailed chemistry. This provides spatially and conditionally resolved variability metrics for reaction-zone quantities (e.g., OH production) and supports a more rigorous interpretation of how hydrogen content modulates chemical sensitivity within otherwise similar global flame regimes.

To complement Eulerian field analysis and to capture three-dimensional transport pathways and time-history effects, this study also employs Lagrangian tracer particles injected from the fuel jet. Lagrangian tracking has precedent in JICF research for relating mixing and dispersion to coherent structures and for quantifying scalar evolution along fluid pathlines; for example, Campolo et al. [22] analyzed dispersion mechanisms in a jet in crossflow using particle tracking, and Esmaeili et al. [23] coupled LES with a stochastic Lagrangian formulation to study scalar mixing in (non-isothermal) JICF. Here, trajectories are conditioned by location and by a narrow band around the stoichiometric mixture fraction to isolate particles traversing the lifted diffusion-flame branch, enabling trajectory-conditioned statistics (e.g., PDFs of scalar dissipation and UQ-derived variability measures) that directly connect flame branch behavior to strain–mixing histories.

The remainder of the paper is organized as follows. Section 2 describes the numerical methodology, operating conditions, and the uncertainty-transfer procedure. Section 3 presents the reacting-flow results, including flame topology, strain-conditioned stabilization, and uncertainty-informed reaction sensitivity. Conclusions are summarized in Section 4.

2. Methodology

2.1. Numerical Solver

High-fidelity numerical simulations are performed using a finite volume solver [24,25] based on block-structured AMR with an embedded boundary (EB) implementation for complex geometry. The compressible Navier–Stokes equations and species transport equations are solved on a 3D Cartesian grid using a second-order spatial discretization and a strong stability-preserving second-order Runge–Kutta scheme for temporal integration. To alleviate the small time-step restriction due to the small cut cells, the state redistribution approach [26,27] is employed. Detailed chemistry is solved using a matrix-based algorithm [28]. The details of the numerics and implementations are discussed in [25]. Differential diffusion effects are represented using a mixture-averaged model, which has been evaluated with the same numerical solver presented in [29,30] for a reacting JICF.

The diffusion velocities can be modeled using various methods, including the mixture-averaged diffusion model and the multicomponent diffusion model. According to the findings presented by Bruno et al. [31], both models produce comparable predictions of fluid-dynamic and thermochemical fields when applied to partially premixed hydrogen jet flames at high Reynolds numbers. However, the mixture-averaged diffusion model distinguishes itself by accommodating variable species diffusivity depending on the composition of the mixture, thus addressing the differential diffusion effects. Such effects contrast with preferential diffusion, where the diffusivity of individual species remains constant regardless of the composition of the mixture. In the context of the current research, where species composition undergoes significant changes due to chemical reactions, the resulting variability in mixture composition requires accounting for differential diffusion effects for accurate predictions. After assessing the balance between computational effort and

numerical accuracy, we selected the mixture-averaged diffusion model as the most suitable method for this investigation. The mixture-averaged diffusion model uses the mass-based mixture-averaged diffusion coefficients matrix, defined as [32]

$$\frac{1}{D_{km}} = \sum_{j \neq k} \frac{X_j}{D_{kj}} + \frac{X_k}{1 - Y_k} \sum_{j \neq k} \frac{Y_j}{D_{kj}}, \tag{1}$$

where D_{kj} is the binary diffusion coefficient matrix. Then the diffusion velocity, $V_{k,i}$, is defined as follows:

$$\begin{aligned} V_{k,i} &= V_{k,i}^{D} + V_{k,i}^{C} \\ &= -\frac{D_{km}}{Y_k} \frac{\partial Y_k}{\partial x_i} + \sum_{k=1}^{N} D_{km} \frac{\partial Y_k}{\partial x_i}, \end{aligned} \tag{2}$$

Due to the modeling of diffusion velocity, the correction velocity, $V_{k,i}^{C}$, is necessary to ensure that $\sum_{k=1}^{N} V_{i,k} \frac{\partial Y_k}{\partial x_i} = 0$.

2.1.1. Lagrangian Particles

Lagrangian particles are continuously injected during the Eulerian simulation to track fluid properties in both time and space. These particles are defined as massless and exhibit perfectly elastic collisions with walls. Particle trajectories evolve based on velocities interpolated from the background gas flow, and their positions are updated at each simulation time step. As particles move from their injection points to the domain exit, they record the history of gas-phase properties directly from the Eulerian cells they encounter. As such, the trajectories of these particles effectively represent pathlines of the Eulerian flow field. These properties are taken directly from the underlying Eulerian cells with no interpolation method used, so the accuracy of the recorded data is inherently tied to the resolution of the Eulerian mesh [33].

For current simulations, the particles were initialized at both D_j below the wall inside the injector and at the crossflow upstream in order to capture both the focusing on the flame behavior and visualize the vortical structures inside the whole JICF system.

2.1.2. Uncertainty Quantification

To incorporate chemistry-driven uncertainty in a mechanism-consistent manner, we leverage the parameter covariance matrix available for the detailed FFCM-2 mechanism [20]. This covariance encodes correlated uncertainties in kinetic parameters and enables forward uncertainty propagation; however, it is specific to FFCM-2 and cannot be applied directly when a reduced mechanism is used for reacting-flow simulations. To verify the applicability of FFCM-2 to hydrogen-fueled conditions, additional details are provided in Appendix C. Further, to verify that the transferred uncertainty does not introduce spurious variability, we compare it against direct uncertainty propagation with the original FFCM-2 mechanism and covariance matrix in a representative counterflow flame; the results are presented in Appendix D.

Accordingly, we employ an uncertainty-transfer procedure (refer to previous work [34] for details). In the present work, the target is a computationally efficient H_2–air mechanism [21]. It is a two-step procedure: first, reduced-manifold states are uniquely reconstructed in full-composition space by initializing trajectories at the unburnt mixing state and integrating forward until a prescribed progress-variable constraint is satisfied. Second, parametric uncertainty is propagated by sampling perturbed reaction-rate coefficients from the mechanism covariance matrices and integrating each realization to the same target state,

thereby generating reaction sensitivity and variability metrics associated with the CFD states. This provides uncertainty-informed measures (e.g., variability in OH production and other reaction-zone quantities) without requiring prohibitively expensive ensemble CFD runs with detailed chemistry.

2.2. Computational Setup

The operating conditions considered in this study are summarized in Table 1, where H_2 (%) denotes the hydrogen content by volume, J is the jet-to-crossflow momentum flux ratio, U_j is the jet bulk velocity, Re_j is the jet Reynolds number, U_c is the crossflow velocity, and Re_c is the crossflow Reynolds number. The baseline configuration consists of a transverse hydrogen jet (H_2–N_2, 70/30 vol.%) at 423 K issuing perpendicularly into a dry-air crossflow ($Y_{O_2} = 0.233$, $Y_{N_2} = 0.767$) at 750 K. The computational domain measures $40 \times 60 \times 80$ mm, and the injector diameter is $D_j = 2$ mm, located $20D_j$ downstream of the inlet. A schematic of the domain and a representative mesh near the injector in the mid-plane are shown in Figure 1. The flow remains subsonic throughout the domain; therefore, Navier–Stokes characteristic boundary conditions with species treatment are imposed at the inflow and outflow boundaries [24]. The relaxation parameters are set to $\sigma = 0.25$ at the outlet and $\eta_i = 3.0$ at the inlet. Turbulent inflow conditions are generated by mapping a homogeneous isotropic turbulence field, following the procedure described in [24,29]. The imposed fluctuations are characterized by a root-mean-square velocity of 5 m/s and a Taylor length scale of $\lambda = 2/k_0 = 0.125$. To initiate ignition, a hot air pocket is introduced near the injection location after the cold turbulent flow field has been stabilized and has reached a statistically steady state; further details are provided in [24]. The adaptive mesh refinement (AMR) tagging criteria are described in Appendix B. Briefly, refinement is driven by the local heat release rate and vorticity magnitude, producing up to five refinement levels along and around the flame front. Grid adequacy is evaluated in Appendix A with respect to both turbulent-flow and flame-front resolution. The estimated flame thickness is approximately 550 μm, corresponding to about 28 cells at the finest resolution of $\Delta = 19.5$ μm. Moreover, comparisons among AMR levels 3, 4, and 5 showed only weak sensitivity to further refinement, and level 4 was therefore considered adequate for resolving the principal flow and flame features of interest. The estimated minimum Kolmogorov length scale is $\eta_k = 18.9$ μm, and the Pope criterion is satisfied for both the level-4 and level-5 cases. Depending on the maximum refinement level, the total cell count is approximately 100, 170, and 230 million for AMR levels 3, 4, and 5, respectively. All simulations were carried out on 3000 cores on a high-performance computing system, with a total computational cost of approximately 300,000 core hours.

Table 1. Operating conditions based on the experiments in [14].

Case	H_2 (%)	J	U_j (m/s)	Re_j	U_c (m/s)	Re_c
A7	70	1.96	100	3000	55	44,000
C7	70	8.41	200	6000	55	44,000
A9	95	1.96	171	2600	55	44,000
C9	95	8.41	342	5200	55	44,000

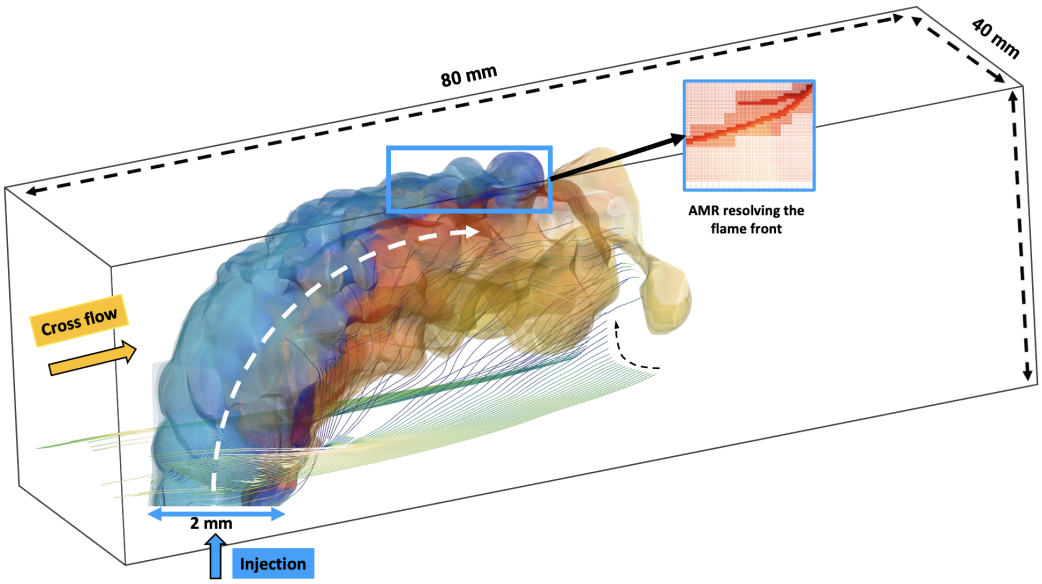


Figure 1. Computational domain with major dimensions. The blue arrow indicates cold fuel injection, the yellow arrow indicates the heated-air cross flow, and the inset shows the refined mesh used to resolve the flame front.

3. Results

3.1. Global Flame Structure

In a previous study [29,30], 70% of cases were validated against experimental results. These prior works showed that the numerical framework provides good agreement with experiments for both the cold-flow field and the reacting flame structure, including the overall flame shape and stabilization behavior. In particular, the predicted flame structure and flame envelope compare well with the experimental observations. In addition, comparison with the LES results shows that the present formulation, including the mixture-averaged transport treatment, is able to capture the flame location in the lee-stabilization zone in the low-speed region. These previous validation results support the reliability of the numerical setup adopted in the present study. This study focuses on the comparison of flame shapes as the hydrogen percentage changes as shown in Figure 2. When the hydrogen content was increased to 95%, the fuel density decreased significantly. To ensure comparable jet characteristics across different fuel compositions, the jet momentum ratio (J) was held constant, necessitating an increase in jet velocity for the lower-density hydrogen-rich mixture. Under this constraint, the jet trajectory remained consistent across the different hydrogen content cases. However, the lower density in the 95% hydrogen case led to greater fluctuations in the fuel stream. This instability contributed to a broader flame spread, driven by the increased volumetric heat release associated with the higher hydrogen content. Notably, the flame continued to exhibit a dual-branch structure, similar to that in the 70% hydrogen case. While the flame front shifted slightly upstream, the location where the two branches connected exhibited both upstream and downstream movement. To further investigate the dynamic behavior of the flame under these conditions, a time-resolved visualization of the flame branches is presented in the following sections.

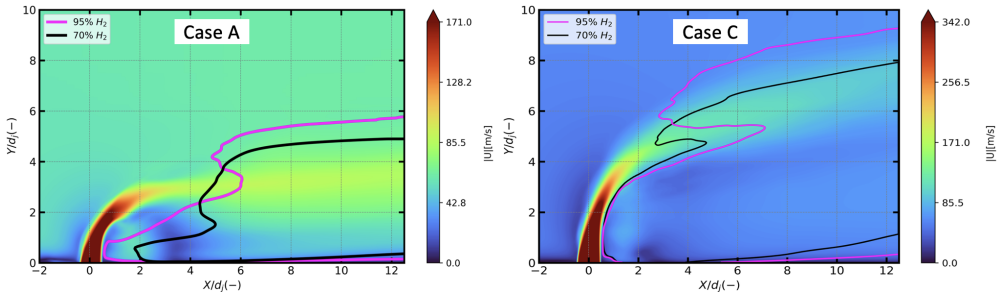


Figure 2. Plot of temporally averaged velocity magnitude in different Cases, and the isoline of Y_{OH} at 10% peak value for 70% and 95% representing the flame shape.

3.2. Strained Flame Front

To visualize the coupled roles of mixing, strain, and chemistry, Figure 3 overlays the flame front on the field of normalized scalar dissipation rate (χ) data and additionally includes the stoichiometric mixture-fraction contour, $Z = Z_{st}$ (black line). This combined view clarifies both where the flame can persist relative to local quenching/undermixing limits and how closely the reacting layer follows the nominal diffusion-flame stoichiometric surface.

The colormap shows the normalized χ values, defined as

$$\hat{\chi} = \frac{\chi}{\chi_{st}^{ext}}, \tag{3}$$

where χ_{st}^{ext} is the stoichiometric χ at extinction obtained from a one-dimensional counterflow calculation in CANTERA [35]. This normalization provides a physically meaningful chemical reference: values $\hat{\chi} \sim \mathcal{O}(1)$ correspond to local mixing/strain intensities comparable to the laminar extinction limit, enabling direct comparisons across cases.

Across all cases, the flame front does not coincide with the maximum-$\hat{\chi}$ regions. Instead, the flame front consistently resides on the immediate low-$\hat{\chi}$ side of the high-$\hat{\chi}$ layer that forms along the primary shear/mixing interface. This indicates stabilization where mixing remains sufficiently strong to bring the mixture toward reactive compositions, yet the local scalar dissipation has relaxed enough for chemical reaction to compete with strain. In the regions of very large $\hat{\chi}$ (orange–magenta), no flame is observed, consistent with conditions approaching or exceeding the extinction reference. Conversely, regions of very small $\hat{\chi}$ (blue–gray) are also largely flame free; although strain is weak there, scalar gradients (and thus interdiffusion toward reactive compositions) are minimal, so the mixture remains close to the unmixed streams. The flame front therefore occupies an intermediate range of χ, bounded by over-strained (high-$\hat{\chi}$) and under-mixed (low-$\hat{\chi}$) zones.

The Z_{st} contour further shows that the lifted branch behaves predominantly as a diffusion flame: the flame front closely follows the stoichiometric surface as it threads along the mixing layer, and the high-$\hat{\chi}$ band intersects the Z_{st} contour in the upstream stabilization region. Notably, the flame front typically appears slightly displaced from the peak-$\hat{\chi}$ ridge and from the Z_{st} line, reflecting finite-rate effects and the fact that the instantaneous reaction zone is set by the local balance between strain effects and chemistry rather than by the mixture fraction alone.

The momentum–flux ratio J sets the dominant changes in flame topology. Comparing $J = 1.96$ (Cases A7 and A9) with $J = 8.41$ (Cases C7 and C9) shows that higher J produces a broader and more contorted high-$\hat{\chi}$ layer and a more pronounced lifted/arched structure, consistent with stronger shear and enhanced turbulent mixing. In contrast, the lower-J cases remain more compact and closer to the lee-stabilized configuration, with a comparatively weaker and lower-lying high-$\hat{\chi}$ ridge. Despite these structural differences, the alignment

of the lifted reaction zone with the stoichiometric surface remains robust: the lifted flame front tracks the Z_{st} contour and resides on the low-$\hat{\chi}$ side of the strongest dissipation.

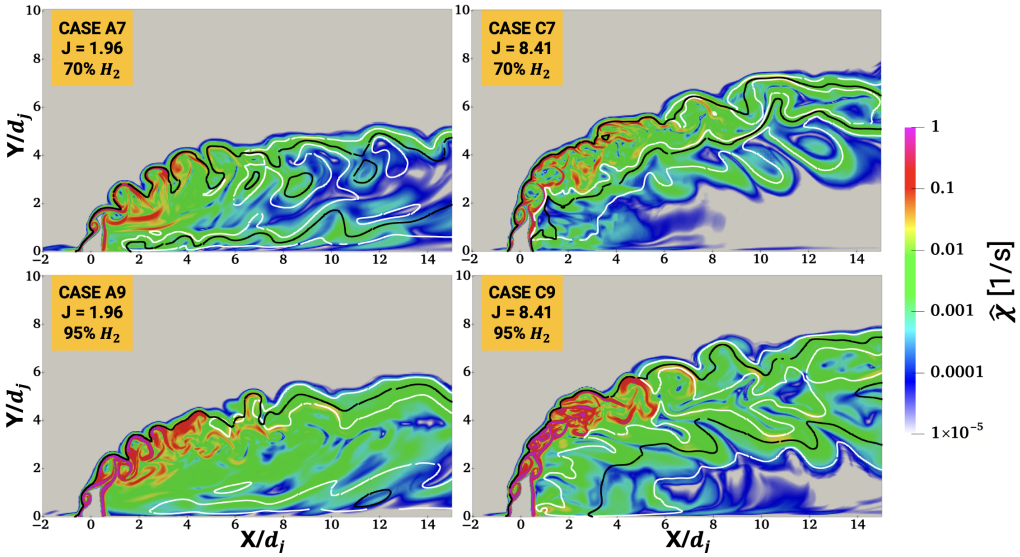


Figure 3. Instantaneous fields of $\hat{\chi} = \chi/\chi_{st}^{ext}$ (log scale) for different cases. The flame front is marked by an iso-contour of Y_{OH} at 10% of its peak value (colored contour), and the black line indicates the stoichiometric mixture-fraction contour $Z = Z_{st}$.

An important exception is observed for the lee-stabilized branch in Case A9, where segments of the flame front do not coincide with the nominal Z_{st} contour yet remain burning. This behavior is consistent with differential-diffusion effects in hydrogen flames. As a result, the reacting layer can appear on the fuel rich side of the nominal Z_{st} line while still attaining locally favorable conditions for reaction (i.e., an effectively closer-to-stoichiometric radical/enthalpy balance at the flame front). This is most evident in the near-wall/recirculation region, where the residence time and differential diffusion can enrich the local fuel content and shift the apparent stoichiometric surface away from the inlet-based Z_{st}.

Overall, using $\hat{\chi}$ normalized by χ_{st}^{ext} together with the Z_{st} contour enables a more rigorous interpretation of stabilization: the flame persists where the flow provides sufficient mixing to reach reactive compositions (often near Z_{st}) while remaining below extinction-level scalar dissipation so that chemistry can overcome local strain.

3.3. Eulerian Chemical State Dynamics

3.3.1. Flame Branch Analysis

Figure 4 presents a comparative analysis of the flame front in chemical space using the Z and Y_{OH}. Scatter plot points, sampled at different times and at a single location for each subplot, are compared against strained and unstrained flame solutions from Cantera [35] at varying strain rates. It should be noted that in the unstrained flame, Y_{OH} is lower than the strained values; however, the temperature of the unstrained flame is higher, as expected. Similarly, the peak temperature aligns with the stoichiometric condition, whereas the maximum Y_{OH} values occur under slightly leaner conditions.

At point A, located at the top edge of the lifted flame branch, for 70% cases, the scatter plot exhibits an ignition–extinction cycle, characterized by an elliptical spread on the lean side near the stoichiometric Z value (Z_{st}). This behavior highlights the presence of intermediate reaction states as fresh gasses mix with combustion products, where ignition and extinction are equally probable. The points of 95% cases follow the theoretical curve more closely and spread on both the lean and rich sides, indicating much better

mixing. At point B, located at the concave region where the lifted and lee-stabilized flame branches connect, the scatter plot shows a trend similar to that at point A. The scatter points mostly stay on the rich side and follow closely the highly strained theoretical curve, indicating the unsteady strain effects from the fuel stream. The 70% case points stayed on the 3000 s^{-1} strained line, while the 95% cases shifted between different strains, indicating more unsteadiness in the 95% cases. At point C, located inside the lee-stabilized flame branch, results from all cases follow the curve of unstrained or low-strained flame because of the low-strain effects in this zone, and the majority of the points are concentrated in a narrow region of Z values, indicating a premixed reaction in this region. However, for case Cs, the scatter points stay on the lean side, while case As stay on the rich side, indicating stronger differential diffusion effects in the lee-stabilized branch side.

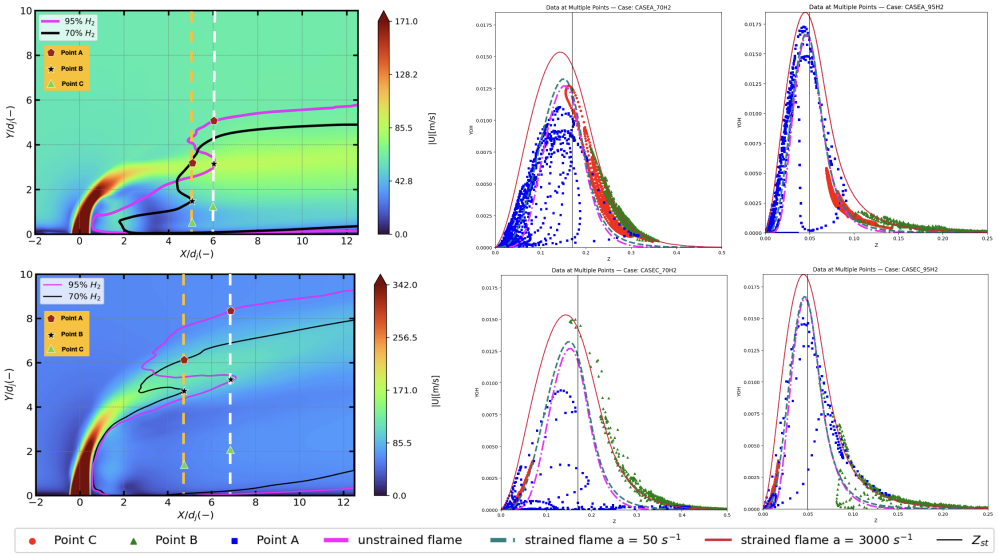


Figure 4. Scatter plot of Y_{OH} versus mixture fraction at sampling locations selected near the flame edge for the different cases. Points A, B, and C are marked on the left panels, while the yellow and white dashed lines indicate the locations of flame edge for the 70% and 95% H_2 cases, respectively. The corresponding Y_{OH}-Z distributions are shown on the right and compared with unstrained and strained flamelet solutions at low strain ($a = 50$ s^{-1}) and high strain ($a = 3000$ s^{-1}).

3.3.2. Reaction Source Variation with Hydrogen Content

Previous sections show that flame characteristics and structure are dominated by the jet momentum ratio, J; varying the hydrogen fraction does not significantly impact the global stabilization mode. All cases remain in the same stable regime with two branches (lee-stabilized and lifted), governed by a strain–chemistry balance and therefore set primarily by J. In this section, we focus on the more subtle chemical-state differences that emerge when kinetic-parameter uncertainty is propagated through the chemistry model.

Figure 5 isolates the lifted branch and visualizes how kinetic uncertainty manifests in the local thermo-chemical state. The scatter points are extracted from a time-averaged mid-plane slice and filtered by both spatial location (lifted branch region) and mixture fraction, selecting points in a narrow band around the stoichiometric value, $|Z - Z_{st}| < 0.05 Z_{st}$ so that the statistics represent the diffusion-flame front associated with the lifted branch. Each point is plotted in (χ, T) space and colored by the relative variation (coefficient of variation) of the OH net production rate inferred from UQ:

$$\beta_{\dot{\omega}_{OH}} = \frac{\sigma(\dot{\omega}_{OH})}{|\mu(\dot{\omega}_{OH})|}, \quad (4)$$

where $\mu(\cdot)$ and $\sigma(\cdot)$ are the mean and standard deviation over the ensemble of kinetic-parameter perturbations generated from the transferred covariance (Section 2.1.2). This diagnostic is used because $\dot{\omega}_{OH}$ is a sensitive marker of H_2–air reaction-zone intensity and directly reflects shifts among chain-branching/termination pathways. For the evaluation of $\beta_{\dot{\omega}OH} = \sigma(\dot{\omega}OH)/|\mu(\dot{\omega}OH)|$, points with $|\mu\dot{\omega}_{OH}| < 10$ were excluded to avoid artificially large values associated with near-zero mean net OH rates.

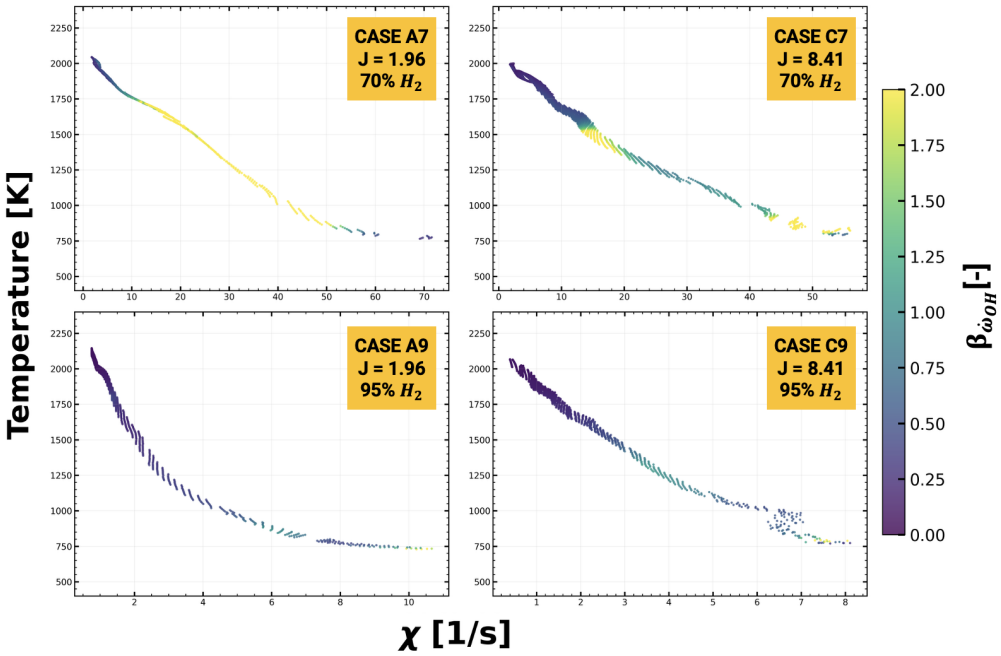


Figure 5. Lifted-branch diffusion-flame-front state space: scatter of temperature T versus χ for four cases (one per panel), extracted from a time-averaged mid-plane slice and filtered by location and $|Z - Z_{st}| < 0.05Z_{st}$. Marker color indicates the net OH production rate variability $\beta_{\dot{\omega}_{OH}} = \sigma(\dot{\omega}_{OH})/|\mu(\dot{\omega}_{OH})|$ from UQ.

The lifted-branch points collapse onto a flamelet-like manifold: higher T occurs at lower χ, while increasing χ corresponds to progressively cooler states approaching local quenching, consistent with the χ-flame front alignment discussed in the previous section. The dominant separation in Figure 5 is composition driven: the 70% H_2 cases populate a substantially higher χ-range than the 95% H_2 cases. This shift can be interpreted through the stoichiometric mixture fraction Z_{st}, which sets where the diffusion flame front can reside relative to the jet shear layer and its vortical structures. Nair et al. [11] emphasize that for small Z_{st} (e.g., H_2–air), the diffusion flame can sit well outside the fuel jet and, hence, outside the shear layer in oxygen-rich environments; correspondingly, modest changes in Z_{st} can move the diffusion flame front toward or away from the shear layer or vortex zone. In the present cases, the lower-hydrogen blend (70% H_2) shifts the stoichiometric surface such that the lifted diffusion-flame front samples more strongly strained/mixed regions associated with the shear-layer dynamics, yielding higher χ. The higher-hydrogen cases (95% H_2) place the lifted diffusion-flame front farther from these regions on average, and the flame therefore samples a lower χ-range.

The UQ-based coloring reveals a clear composition dependence in reaction sensitivity. The 70% H_2 cases (A7, C7) exhibit markedly larger $\beta_{\dot{\omega}_{OH}}$ over much of the lifted-branch manifold, especially at intermediate T and moderate-to-high χ, whereas the 95% H_2 cases (A9, C9) remain predominantly low-variation. This difference is consistent with the higher-χ, more strain-affected thermo-chemical states sampled by the 70% lifted branch, where the flame more frequently resides in intermediate chemical states with a weaker and less

robust radical pool. Based on the reaction contribution ranking obtained from Cantera at representative states along the lifted-flame branch, we hypothesize that, under these conditions, OH production in the 70% cases is more sensitive to the three-body recombination pathway $H + O + M \rightleftharpoons OH + M$. We do not suggest that this pathway is uniquely important only in the 70% cases; rather, its relative contribution to local OH production appears to become larger in the 70% lifted branch, where the radical pool is less fully developed and recombination pathways may play a more important role in sustaining OH. Under this interpretation, perturbations to this reaction rate would be expected to produce larger changes in $\dot{\omega}_{OH}$, consistent with the elevated $\beta_{\dot{\omega}_{OH}}$ observed in the 70% cases. By contrast, the 95% H_2 lifted branch samples lower χ and appears to remain in a more chemically robust state, so OH production may be less dependent on this recombination-mediated pathway and may therefore exhibit smaller variability. To confirm these findings, a more rigorous analysis will be conducted in the future to establish the attribution of the observed variability to specific reaction pathways.

3.4. Lagrangian Chemical State Dynamics

The Eulerian state-space analysis above provides a compact view of lifted-branch chemical sensitivity, but it does not capture the inherently three-dimensional transport pathways and the time history by which fluid elements reach, interact with, and traverse the lifted diffusion flame front. To address this, Lagrangian tracer particles are injected from the jet stream and tracked over time. Particles passing through the lifted branch are identified and selected using the same physical conditioning used for Figure 5, namely spatial filtering in the lifted branch region, together with a narrow band around the stoichiometric mixture fraction and also the same threshold for $\beta_{\dot{\omega}_{OH}}$. For each case, 36,000 massless Lagrangian tracer particles are injected and tracked over one flow-through time. Of these, 8000 particles are randomly selected and used for data processing and statistical analysis. The subset contributing to the lifted-branch conditioned statistics is case dependent but is typically on the order of 10^2. Accordingly, the conditioned PDFs shown below should be interpreted primarily as comparative distributions under a consistent sampling procedure rather than as fully converged asymptotic statistics.

Before examining the trajectory-conditioned statistics, it is useful to consider the particle motion itself. Figure 6 shows representative lifted-branch trajectories for Case C7, colored by temperature. The trajectories indicate that fluid elements do not follow a single monotonic route toward the lifted flame front. Instead, several transport pathways are observed, including direct convection into the lifted branch, lateral spreading within the shear layer, and recirculation-driven looping near the lee side of the jet. In particular, the side view and three-dimensional view show that some particles enter the recirculation zone, undergo partial reaction there, and are subsequently re-entrained into the colder fuel stream. This process can return heat, radicals, and partially reacted species to the low-temperature jet fluid before it reaches the lifted branch. Such recirculation-mediated radical feedback is observed in all cases, although its extent depends on the flow conditions. These trajectories, therefore, show that the lifted diffusion flame front is shaped not only by the instantaneous local state but also by the prior thermo-chemical history of the fluid elements feeding it.

Motivated by these distinct transport histories, trajectory-conditioned probability density functions (PDFs) were constructed using the instantaneous $\chi(t)$ and the net OH production rate variability $\beta_{\dot{\omega}_{OH}}(t) = \frac{\sigma(\dot{\omega}_{OH})}{|\mu(\dot{\omega}_{OH})|}$. For both figures, the PDF bin widths were determined using Knuth's rule, which provides a Bayesian, data-driven criterion for selecting the optimal histogram binning [36,37]. Figure 7 shows the lifted-branch PDFs of $\beta_{\dot{\omega}_{OH}}$. The 70% H_2 cases (A7, C7) exhibit broad distributions with substantial probability

extending to large $\beta_{\dot{\omega}_{OH}}$, demonstrating that OH production along lifted-branch trajectories is strongly influenced by kinetic-parameter uncertainty over a wide range of sampled conditions. In contrast, the 95% H_2 cases (A9, C9) collapse to narrow peaks at relatively small $\beta_{\dot{\omega}_{OH}}$ with only weak high-β tails, providing trajectory-based confirmation that the lifted diffusion flame front is markedly less sensitive to kinetic uncertainty at a higher hydrogen fraction.

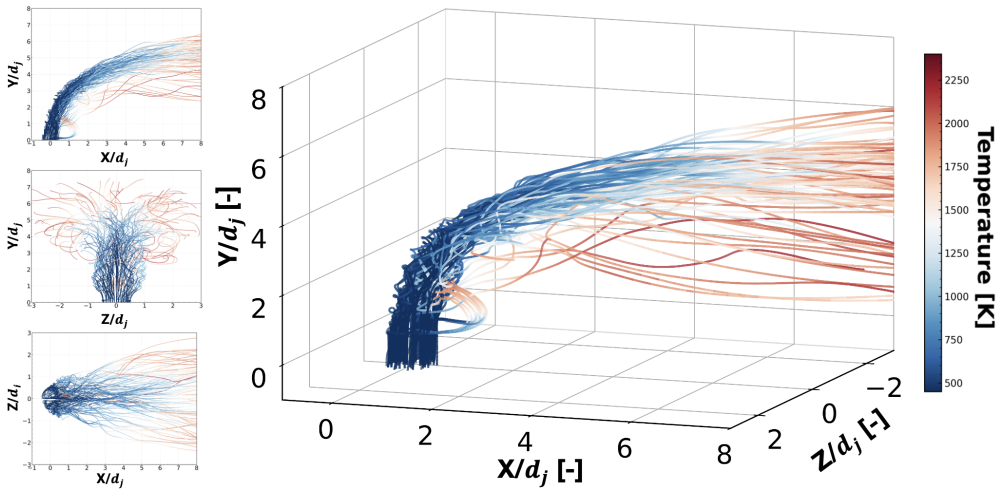


Figure 6. Representative lifted-branch tracer-particle trajectories for CASE C7, shown in multiple views and colored by temperature.

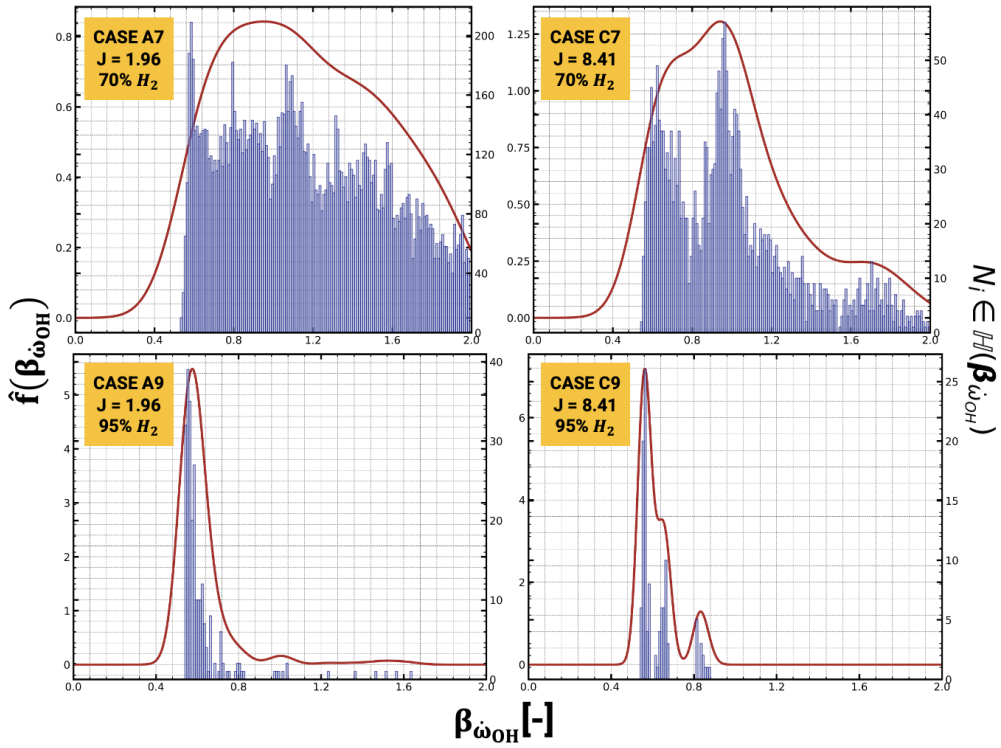


Figure 7. Lifted-branch diffusion-flame-front PDFs of net OH production rate variability, $\beta_{\dot{\omega}_{OH}} = \sigma(\dot{\omega}_{OH})/|\mu(\dot{\omega}_{OH})|$. Red curve: estimated PDF $\hat{f}(\beta_{\dot{\omega}_{OH}})$ (left axis). Blue bars: sample counts N_i in each histogram bin $H(\beta_{\dot{\omega}_{OH}})$ (right axis).

An additional feature of Figure 7 is that the higher-J cases (C7 and C9) exhibit a bimodal or shoulder-like distribution in $\beta_{\dot{\omega}_{OH}}$, whereas the lower-$J$ cases (A7 and A9) remain predominantly unimodal. This likely reflects the broader range of trajectory histories sampled by the lifted branch at high J. In the C-cases, stronger shear-layer dynamics

and greater three-dimensional intermittency allow particles reaching the lifted branch to separate into two characteristic groups: one that passes through more strongly strained, partially reacted states with larger OH-production variability, and another that reaches the branch after experiencing more relaxed mixing histories with lower variability. The A-cases, by contrast, exhibit a more compact lifted branch and a narrower range of strain–mixing histories, so the selected particles populate a single dominant thermo-chemical state and produce only one main peak in $\beta_{\dot{\omega}_{OH}}$.

Figure 8 reports the corresponding lifted-branch PDFs of the χ. In direct agreement with Figure 5 and the flame–χ alignment discussed previously, the 95% H_2 cases (A9, C9) are strongly concentrated at low χ, indicating that fluid elements reaching the lifted diffusion flame front predominantly experience weaker scalar-gradient dissipation along their histories. The 70% H_2 cases (A7, C7), by comparison, populate a substantially higher χ-range and exhibit broader distributions with pronounced high-χ tails, showing that the lifted diffusion flame front at lower hydrogen fraction more frequently resides in, or is fed by, strongly strained/mixed environments. This behavior is consistent with the stoichiometric-surface positioning argument noted by Nair et al. [11]: changes in Z_{st} can shift the diffusion flame front relative to the jet shear layer and associated vortical structures, thereby changing the χ levels sampled by the lifted branch. While J modulates the detailed PDF shapes through three-dimensional mixing and shear-layer intermittency, the dominant separation between the 70% and 95% H_2 remains the shift of probability mass toward higher χ for the 70% cases.

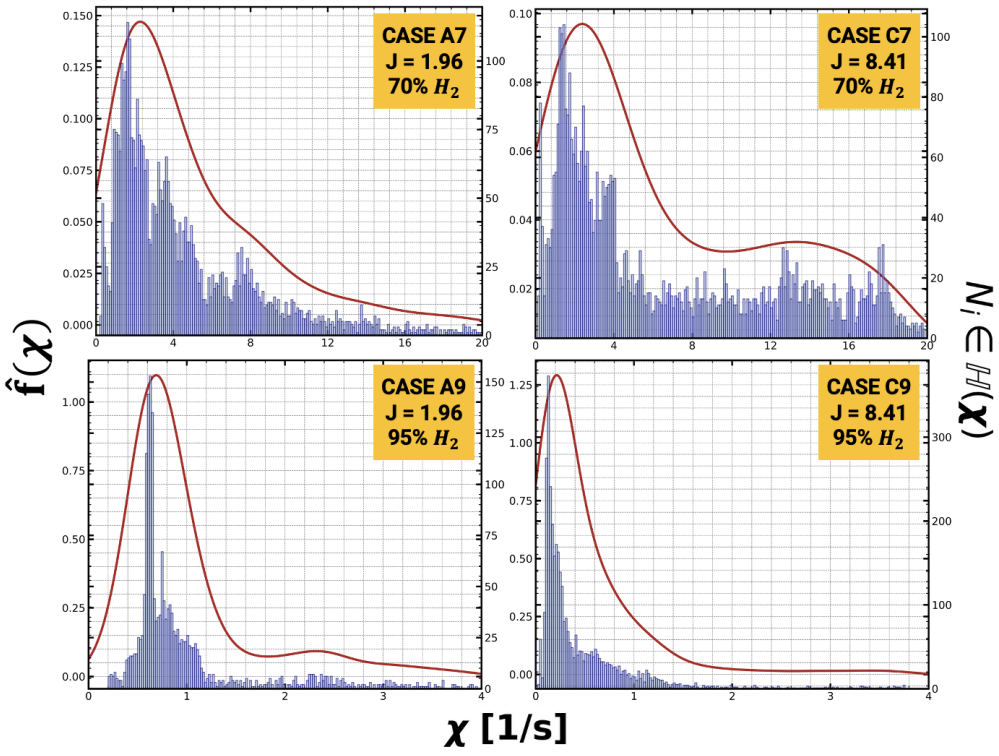


Figure 8. Lifted-branch diffusion-flame-front PDFs of χ (s^{-1}). Red curve: estimated PDF $\hat{f}(\chi)$ (left axis). Blue bars: sample counts N_i in each histogram bin $H(\chi)$ (right axis).

Taken together, the trajectory visualization and the Eulerian/Lagrangian statistics establish a consistent picture: although J controls the macroscopic stabilization and flame topology, hydrogen content systematically modulates both the scalar-dissipation environment sampled by the lifted diffusion flame front and the sensitivity of radical-production chemistry to kinetic-parameter uncertainty. The lower sensitivity and lower χ exposure in

the 95% H_2 cases imply the greater chemical robustness and improved predictive reliability of OH-based reaction-zone metrics, whereas the 70% H_2 cases operate more frequently in higher-χ conditions and exhibit amplified kinetic sensitivity. The observed recirculation-mediated return of partially reacted fluid to the cold jet further emphasizes that the lifted branch is sustained by both the local strain–chemistry balance and nonlocal trajectory history, motivating uncertainty-aware interpretation for lower-H_2 blends.

4. Conclusions

This study examined turbulent reacting jets in crossflow relevant to staged hydrogen fueling, focusing on strain-conditioned stabilization and chemistry-driven uncertainty. High-fidelity simulations with adaptive mesh refinement were performed using mixture-averaged transport, and correlated kinetic uncertainty was incorporated via a covariance-transfer/refinement procedure from a detailed mechanism to a reduced H_2–air mechanism.

Across all cases, the macroscopic flame topology remained in a stable two-branch regime (lee-stabilized and lifted) and was governed primarily by the jet momentum–flux ratio J. Analysis of the normalized χ showed that the flame front consistently occupies a transitional zone: it lies on the low-dissipation side of intense mixing layers, while both very high χ (over-strained) and very low χ (under-mixed) regions are flame free. The stoichiometric contour further indicated that the lifted branch behaves predominantly as a diffusion flame, with localized departures in the recirculation zones attributable to preferential/differential diffusion. While hydrogen content did not change the global stabilization mode, uncertainty-informed diagnostics revealed clear composition-dependent differences in the lifted branch. Both Eulerian (χ, T) state-space analysis and trajectory-conditioned tracer statistics showed that higher-hydrogen cases sample lower χ and exhibit substantially reduced variability in OH production under kinetic perturbations, whereas lower-hydrogen blends experience higher dissipation and amplified chemical sensitivity. These results emphasize that J controls the global flow–flame structure, while hydrogen content primarily modulates local chemical robustness and the sensitivity of reaction-zone markers. From a modeling standpoint, the findings motivate mechanism-consistent UQ for reduced-chemistry simulations, especially for blends that push the lifted branch toward higher-χ environments.

From a design and operation perspective, practical combustors often undergo dynamic fuel staging, in which the H_2 fraction is varied to satisfy changing load demands. The present results show that, when J is held constant, increasing the H_2 fraction produces smaller variations in the lifted-flame branch, consistent with a shift from a fluid-strain-controlled regime toward one in which flame heat release promotes local flow laminarization and greater branch-to-branch robustness. In contrast, lower-H_2 blends sample higher-χ environments and exhibit greater sensitivity of OH production to kinetic uncertainty, indicating that these conditions require particular care in reduced-chemistry modeling and uncertainty quantification. From an operational-safety standpoint, the results also suggest that if J decreases while the H_2 fraction increases, richer burning in the lee branch can promote localized hot spots. Although flashback and wall-heating are not addressed directly in the present configuration, such behavior is relevant to combustor safety because it may increase thermal loading, reduce material margins, and signal operating conditions that are more susceptible to undesirable flame migration or excessive local heat release. Overall, the present study provides guidance for both combustor design and model development: the momentum–flux ratio remains the primary control parameter for global flame topology, whereas mechanism-consistent UQ becomes especially important for lower-H_2 blends whose lifted branches are exposed to higher-χ conditions and therefore show greater chemical sensitivity.

https://doi.org/10.3390/hydrogen7020056

Author Contributions: S.Z. performed the simulations, analyzed the data, and wrote the first draft of the manuscript. V.S. performed the simulations, helped design the research, performed data analysis, and edited the manuscript. V.R. helped design the research, oversaw research activities, and edited the manuscript. All authors have read and agreed to the published version of the manuscript.

Funding: The authors acknowledge financial support from the DOE UTSR program under grant number DE–FOA-0002397 (project number FE0032076), with Dr. Richard P. Dalton as program monitor.

Institutional Review Board Statement: Not applicable.

Informed Consent Statement: Not applicable.

Data Availability Statement: The data that support the findings of this study are available from the corresponding author upon reasonable request.

Conflicts of Interest: The authors declare no conflicts of interest. The funders had no role in the design of the study; in the collection, analyses, or interpretation of data; in the writing of the manuscript; or in the decision to publish the results.

Appendix A. Grid Convergence

A primary requirement of the AMR framework is the accurate representation of localized structures of interest, which in the present case is the flame front. For the wall-bounded turbulent flow and the associated boundary-layer resolution, the wall-unit spacing was estimated as $y^+ = 0.66$ from the simulation data using $y^+ = \frac{u_\tau \delta}{\nu}$ [38]. Here, the friction velocity is given by $u_\tau = \sqrt{\frac{\tau_w}{\rho}}$, while the wall shear stress is evaluated as $\tau_w = \rho\nu\left(\frac{d\tilde{U}}{dy}\right)_{y=0}$ from the wall-normal gradient of the Favre-averaged streamwise velocity. To assess flame resolution, the flame thickness was estimated to be approximately 550 μm by considering a premixed one-dimensional flame at a comparable mixture composition. At the finest mesh employed here, corresponding to five AMR levels with $\Delta = 19.5$ μm, the flame thickness is resolved by 28 computational cells, which is sufficient to capture the flame surface, although an even finer mesh may be required to fully represent turbulence–chemistry interactions. To examine this sensitivity, three independent calculations were performed using AMR levels 3, 4, and 5. As shown in Figure A1, the temporally averaged density and its standard deviation remain closely matched across the different refinement levels, indicating weak sensitivity of the bulk solution to additional refinement. Based on these results, level 4 refinement is considered adequate for resolving the principal flow and flame features of interest. Although increasing spatial resolution improves the representation of certain small-scale structures, the overall system response, in terms of thermodynamic quantities, is not significantly altered once the flame is sufficiently resolved. Furthermore, the DNS data were used to evaluate the turbulent dissipation rate as $\epsilon = 2\nu\widetilde{S'_{ij}S'_{ij}}$, using the Favre-averaged fluctuating strain-rate tensor. The Kolmogorov length scale was then estimated from $\eta_k = \left(\nu^3/\epsilon\right)^{1/4}$. Taking the minimum value over several microseconds after the flow reached steady state gave $\eta_k = 18.9$ μm. For DNS resolution, the Pope criterion [38], $\frac{\Delta}{\eta} = \frac{\pi}{1.5}$, is satisfied for both the 4-level and 5-level AMR cases.

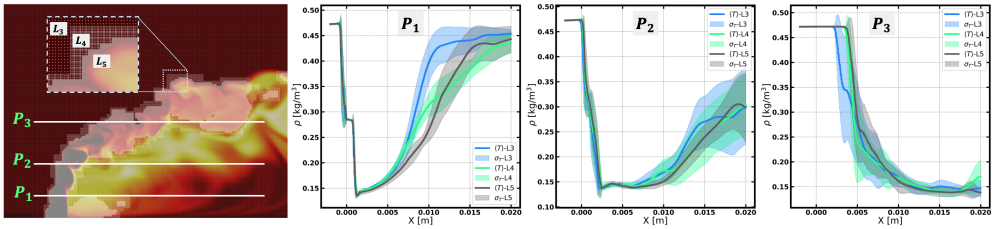


Figure A1. Temporally averaged density profiles with corresponding standard deviations extracted along the three lines indicated in the mid-plane contour of the simulation for three independently refined grids (see inset). Results for AMR level 3 are shown in blue, level 4 in green, and level 5 in gray.

Appendix B. AMR Tagging Criteria

The AMR implementation employs a block-structured hierarchy in which each spatial region may contain multiple refinement levels with a fixed refinement ratio. Information is exchanged across levels such that the coarse-grid solution is conservatively corrected to match the total conserved quantity represented by the ensemble of embedded fine cells. The tagging criteria used to identify regions requiring mesh adaptation are summarized here. The left panel of Figure A2 emphasizes the flame-front structure through the heat release rate (HRR) field, which is used as a primary indicator for refinement. Cells with HRR $> 2 \times 10^9$ J/(s $\cdot$ m^3) are tagged for level 4 and above, while regions with vorticity magnitude exceeding 1×10^5 s^{-1} are tagged for level 3 and above. As a result, five levels of refinement are established along and around the flame front.

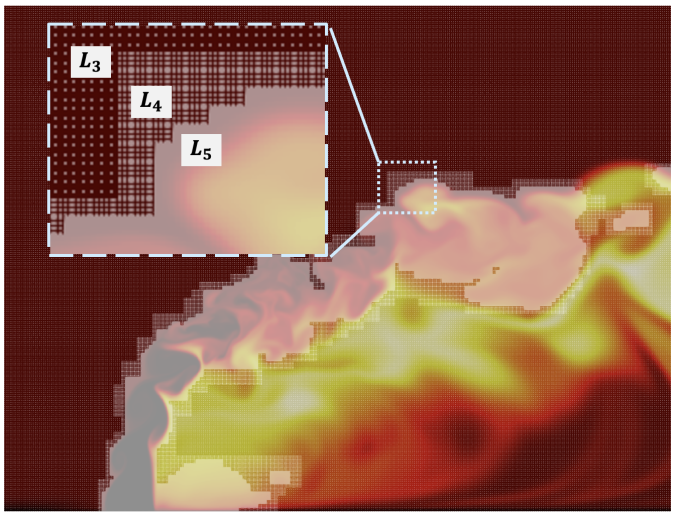


Figure A2. Contour plot of a temperature field showing AMR level (blocks) tagging.

Appendix C. H_2 Reactions with FFCM-2

In the present study, the FFCM-2 mechanism and its associated covariance matrix are adopted to analyze H_2 oxidation chemistry. Because this application is not entirely straightforward, an initial validation step is performed by evaluating the ignition delay time (IDT) for a system containing hydrogen as the sole fuel component. Figure A3 presents a comparison of the H_2 IDT predicted by FFCM-2 and by the dedicated H_2 mechanism of Mueller et al. [21], with ignition defined using the $\left.\frac{dT}{dt}\right|_{\max}$ criterion under the same thermochemical conditions. Over the full temperature interval examined, the IDT trend obtained with FFCM-2 remains in close agreement with that predicted by the H_2 mechanism, with discrepancies that are minor relative to the overall temperature-dependent variation in IDT, which spans several orders of magnitude. Furthermore, the FFCM-2 predictions remain within the reported uncertainty envelope, defined here by

the 0.001–0.999 quantiles, while the alternative H_2 mechanism also lies largely within this band. This level of agreement supports the use of FFCM-2 for H_2 reaction studies under the present conditions, as it reproduces the ignition-delay behavior of the reference hydrogen mechanism without introducing a significant systematic offset in the IDT prediction.

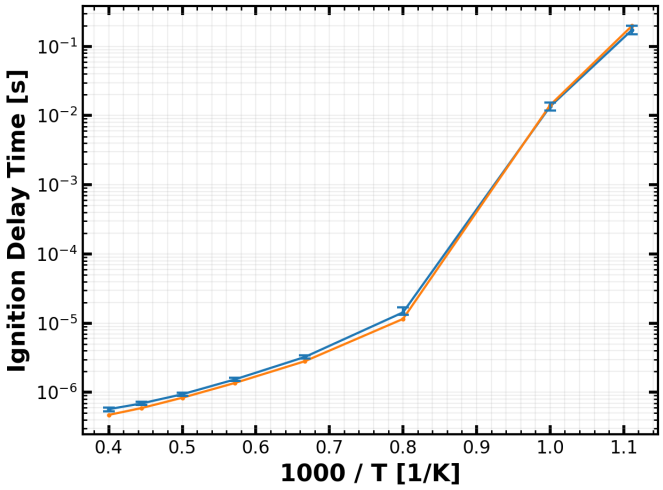


Figure A3. Comparison of ignition delay time (log scale) for H_2 at $P = 10$ atm and $\phi = 0.5$ as a function of inverse temperature, $1000/T$. Predictions obtained using the FFCM-2 mechanism (–) are shown alongside those from the H_2 mechanism [21] (–). The bars denote the uncertainty bounds associated with the FFCM-2 predictions.

Appendix D. Validation of the Uncertainty-Transfer Procedure Against Direct FFCM-2 Propagation

To assess whether the variability predicted by the transferred-UQ framework could arise from the mapping/reduction procedure itself, we performed an additional canonical validation using a steady 1D counterflow flame at fuel composition and strain-rate conditions relevant to the present JICF study. In this case, uncertainty was propagated directly with the detailed FFCM-2 mechanism and its associated covariance matrix [20], without applying the transfer procedure. This comparison serves a specific purpose. The covariance information is available only for FFCM-2, whereas the reacting-flow simulations in the main study employ the reduced H_2–air mechanism of Mueller et al. [21]. As discussed in the main text, the uncertainty-transfer methodology allows the chemistry uncertainty encoded in FFCM-2 to be mapped onto reduced-manifold CFD states in a mechanism-consistent way; see ref. [34] for details. The present counterflow calculation provides a direct reference case using the original detailed chemistry and, therefore, serves as a validation check on whether the transferred-UQ framework produces variability consistent with the parent mechanism.

Figures A4 and A5 show the uncertainty envelopes obtained from the direct FFCM-2 propagation for temperature and $\dot{\omega}_{OH}$, respectively, plotted against Bilger mixture fraction Z. In both cases, the baseline solution lies very close to the central tendency of the ensemble, and the uncertainty bands remain relatively modest across the flame structure, including in the vicinity of the stoichiometric mixture fraction. These results indicate that the chemistry uncertainty encoded by the original FFCM-2 covariance does not generate anomalous variability in this canonical flame configuration.

To further examine whether large OH-production variability can emerge under extinction-sensitive conditions, we also performed additional steady counterflow calculations in which the strain rate was increased toward the corresponding extinction limit for the relevant fuel cases. In these near-extinction counterflow flames, the direct FFCM-2

ensemble exhibits substantially amplified variability in $\dot{\omega}_{OH}$, particularly in the vicinity of the stoichiometric mixture fraction. As shown in Figure A6, the uncertainty envelope broadens markedly as the flame approaches extinction, with relative variation becoming order-unity in some regions. This provides a qualitative indication that the large variability observed in OH production under the lifted-flame conditions is physically plausible near extinction and is not solely a consequence of the uncertainty-transfer procedure.

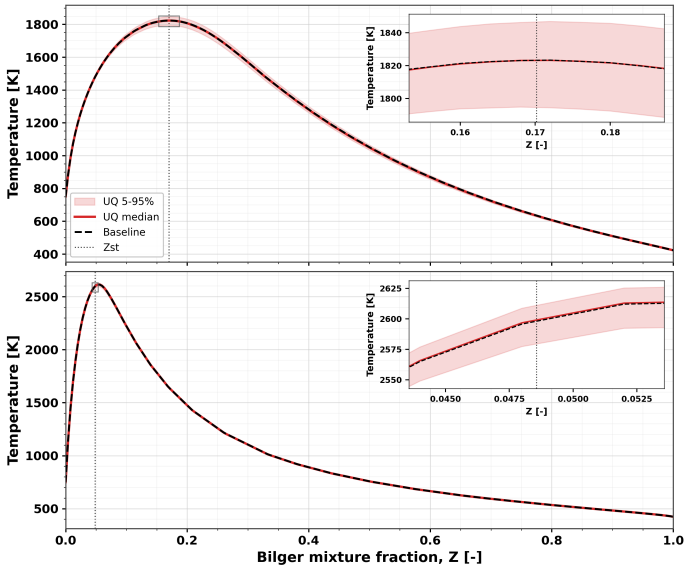


Figure A4. Direct uncertainty propagation using the original FFCM-2 mechanism and covariance matrix for a representative counterflow flame at JICF relevant conditions. The upper panels show the 70% H_2 case, whereas the lower panels show the 95% H_2 case. Temperature is shown as a function of Bilger mixture fraction Z. The shaded region denotes the 5% to 95% interval, the red solid line denotes the ensemble median, and the black dashed line denotes the baseline solution. Insets highlight the uncertainty level near the stoichiometric mixture fraction.

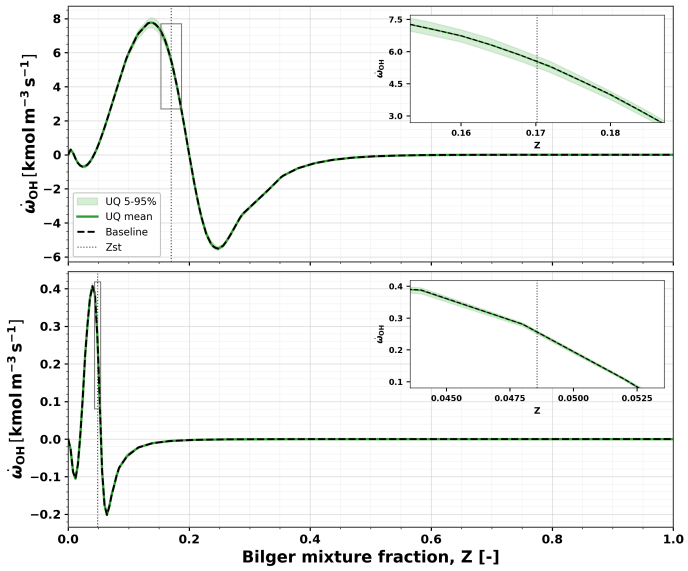


Figure A5. Direct uncertainty propagation using the original FFCM-2 mechanism and covariance matrix for the same representative counterflow flame as in Figure A4. The upper panels show the 70% H_2 case, whereas the lower panels show the 95% H_2 case. The OH production rate $\dot{\omega}_{OH}$ is shown as a function of Bilger mixture fraction Z. The shaded region denotes the 5% to 95% interval, the green solid line denotes the ensemble mean, and the black dashed line denotes the baseline solution. Insets highlight the uncertainty level near the stoichiometric mixture fraction.

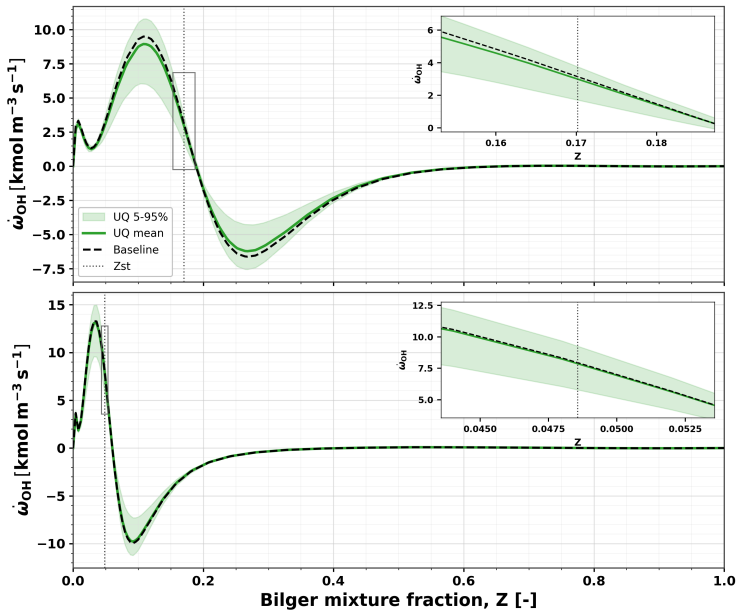


Figure A6. Direct uncertainty propagation using the original FFCM-2 mechanism and covariance matrix for a counterflow flame at strain rates approaching the steady extinction limit. The upper panels show the 70% H_2 case, whereas the lower panels show the 95% H_2 case. The OH production rate $\dot{\omega}_{OH}$ is plotted as a function of Bilger mixture fraction Z. The shaded region denotes the 5% to 95% interval, the green solid line denotes the ensemble mean, and the black dashed line denotes the baseline solution. Insets highlight the uncertainty level near the stoichiometric mixture fraction. The broadening of the uncertainty band demonstrates that OH-production variability increases substantially as the steady flame approaches extinction.

This validation supports the conclusion that the larger variability observed in the lifted-flame analysis, particularly in $\beta_{\dot{\omega}_{OH}}$ for the 70% H_2 cases, is not an artifact of the uncertainty-transfer procedure itself. At the same time, the limitations of the canonical configuration should be kept in mind. A steady counterflow flame does not reproduce the unsteady recirculation, lifted-branch motion, or intermittent near-extinction behavior present in the JICF configuration. In addition, for a given steady counterflow configuration, extinction is approached through a single threshold in strain rate, whereas the lifted branch in the full reacting-flow simulation samples a broader unsteady state space. Therefore, while the counterflow results validate the mechanism consistency of the UQ framework and provide a useful near-extinction reference, they do not fully represent the dynamical flame-state sensitivity sampled along the lifted branch in the full reacting-flow simulations.

References

1. Goldmeer, J. *Power to Gas: Hydrogen for Power Generation—Fuel Flexible Gas Turbines as Enablers for a Low or Reduced Carbon Energy Ecosystem*; General Electric: Boston, MA, USA, 2019.
2. Vandervort, C.; Leach, D.; Walker, D.; Sasser, J. Commercialization and Fleet Experience of the 7/9HA Gas Turbine Combined Cycle. In *Proceedings of the ASME Turbo Expo: Power for Land, Sea, and Air*; Paper V003T08A006; ASME: New York, NY, USA, 2019.
3. Martin, S.M.; Ahmed, K.A.; Genova, T. *Improving NOx Entitlement with Axial Staging*; Embry-Riddle Aeronautical University: Daytona Beach, FL, USA, 2018.
4. Jiang, X.; Tang, Y.; Liu, Z.; Raman, V. Computational modeling of boundary layer flashback in a swirling stratified flame using a LES-based non-adiabatic tabulated chemistry approach. *Entropy* **2021**, *23*, 567. [CrossRef] [PubMed]
5. Kolla, H.; Grout, R.; Gruber, A.; Chen, J.H. Mechanisms of flame stabilization and blowout in a reacting turbulent hydrogen jet in cross-flow. *Combust. Flame* **2012**, *159*, 2755–2766. [CrossRef]
6. Hochgreb, S. Mind the gap: Turbulent combustion model validation and future needs. *Proc. Combust. Inst.* **2019**, *37*, 2091–2107. [CrossRef]
7. Sharma, V.; Tang, Y.; Raman, V. Stabilization of Hydrogen-enriched Jet Flames in a Crossflow. In *AIAA SCITECH 2024 Forum, Orlando, FL, USA, 8–12 January 2024*; Paper 0393; AIAA: Reston, VA, USA, 2024.

8. Berger, L.; Attili, A.; Pitsch, H. Synergistic interactions of thermodiffusive instabilities and turbulence in lean hydrogen flames. *Combust. Flame* **2022**, *244*, 112254. [CrossRef]
9. Tang, H.; Yang, C.; Krishna, Y.; Wang, G.; Roberts, W.L.; Guiberti, T.F.; Magnotti, G. Differential diffusion effects in the near field of non-premixed $NH_3/H_2/N_2$-air jet flames at elevated pressure. *Exp. Therm. Fluid Sci.* **2023**, *149*, 111020. [CrossRef]
10. Minamoto, Y.; Kolla, H.; Grout, R.W.; Gruber, A.; Chen, J.H. Effect of fuel composition and differential diffusion on flame stabilization in reacting syngas jets in turbulent cross-flow. *Combust. Flame* **2015**, *162*, 3569–3579. [CrossRef]
11. Nair, V.; Sirignano, M.; Emerson, B.L.; Lieuwen, T.C. Combustion and flame position impacts on shear layer dynamics in a reacting jet in cross-flow. *J. Fluid Mech.* **2022**, *942*, A41. [CrossRef]
12. Nair, V.; Sirignano, M.; Emerson, B.L.; Lieuwen, T.C. Near-field evolution and scaling of shear layer instabilities in a reacting jet in crossflow. *J. Fluid Mech.* **2023**, *960*, A13. [CrossRef]
13. Grout, R.W.; Gruber, A.; Yoo, C.S.; Chen, J.H. Direct numerical simulation of flame stabilization downstream of a transverse fuel jet in cross-flow. *Proc. Combust. Inst.* **2011**, *33*, 1629–1637. [CrossRef]
14. Steinberg, A.M.; Sadanandan, R.; Dem, C.; Kutne, P.; Meier, W. Structure and stabilization of hydrogen jet flames in cross-flows. *Proc. Combust. Inst.* **2013**, *34*, 1499–1507. [CrossRef]
15. Raman, V.; Hassanaly, M. Emerging trends in numerical simulations of combustion systems. *Proc. Combust. Inst.* **2019**, *37*, 2073–2089. [CrossRef]
16. Mueller, M.E.; Iaccarino, G.; Pitsch, H. Chemical kinetic uncertainty quantification for large eddy simulation of turbulent nonpremixed combustion. *Proc. Combust. Inst.* **2013**, *34*, 1299–1306. [CrossRef]
17. Ji, W.; Wang, J.; Zahm, O.; Marzouk, Y.M.; Yang, B.; Ren, Z.; Law, C.K. Shared low-dimensional subspaces for propagating kinetic uncertainty to multiple outputs. *Combust. Flame* **2018**, *190*, 146–157. [CrossRef]
18. Cai, F.; Zhou, H.; Yao, M.; Ren, Z. Exploiting active subspace for modeling uncertainty and optimization in fan-shaped film cooling simulation. In *Proceedings of the ASME Turbo Expo: Power for Land, Sea, and Air*; Paper V007T12A037; ASME: New York, NY, USA, 2024; Volume 87998.
19. Wang, N.; Yang, T.; Ren, Z. Active subspace variation and modeling uncertainty in a supersonic flame simulation. *AIAA J.* **2021**, *59*, 1798–1807. [CrossRef]
20. Zhang, Y.; Dong, W.; Vandewalle, L.; Xu, R.; Smith, G.; Wang, H. Foundational Fuel Chemistry Model Version 2.0 (FFCM-2). 2023. Available online: https://web.stanford.edu/group/haiwanglab/FFCM2 (accessed on 10 March 2026).
21. Mueller, M.A.; Kim, T.J.; Yetter, R.A.; Dryer, F.L. Flow reactor studies and kinetic modeling of the H_2/O_2 reaction. *Int. J. Chem. Kinet.* **1999**, *31*, 113–125. [CrossRef]
22. Campolo, M.; Salvetti, M.V.; Soldati, A. Mechanisms for Microparticle Dispersion in a Jet in Crossflow. *AIChE J.* **2005**, *51*, 28–43. [CrossRef]
23. Esmaeili, M.; Afshari, A.; Jaberi, F.A. Turbulent mixing in non-isothermal jet in crossflow. *Int. J. Heat Mass Transf.* **2015**, *89*, 1239–1257. [CrossRef]
24. Zhang, S.; Sharma, V.; Sharma, S.; Bielawski, R.; Raman, V. Characteristic Boundary Condition for Embedded-Boundary Method Based Compressible Reacting Flow Solver. In *AIAA AVIATION 2024 Forum, Las Vegas, NV, USA, 29 July–2 August 2024*; AIAA: Reston, VA, USA, 2024.
25. Sharma, S.; Bielawski, R.; Gibson, O.; Zhang, S.; Sharma, V.; Rauch, A.H.; Singh, J.; Abisleiman, S.; Ullman, M.; Barwey, S.; et al. An AMReX-based Compressible Reacting Flow Solver for High-speed Reacting Flows Relevant to Hypersonic Propulsion. *arXiv* **2024**, arXiv:2412.00900.
26. Berger, M.; Giuliani, A. A state redistribution algorithm for finite volume schemes on cut cell meshes. *J. Comput. Phys.* **2021**, *428*, 109820. [CrossRef]
27. Giuliani, A.; Almgren, A.S.; Bell, J.B.; Berger, M.J.; de Frahan, M.T.H.; Rangarajan, D. A weighted state redistribution algorithm for embedded boundary grids. *J. Comput. Phys.* **2022**, *464*, 111305. [CrossRef]
28. Barwey, S.; Raman, V. A Neural Network-Inspired Matrix Formulation of Chemical Kinetics for Acceleration on GPUs. *Energies* **2021**, *14*, 2710. [CrossRef]
29. Zhang, S.; Sharma, V.; Raman, V. Differential Diffusion Effects on Hydrogen-Enriched Jet Flames in a Crossflow. In *AIAA SCITECH 2025 Forum, Orlando, FL, USA, 6–10 January 2025*; Paper 0154; AIAA: Reston, VA, USA, 2025.
30. Zhang, S.; Sharma, V.; Raman, V. High-fidelity numerical analyses for hydrogen jet-flames in crossflow. In *Proceedings of the ASME Turbo Expo*; Paper V03BT04A052; ASME: New York, NY, USA, 2025; Volume 88797.
31. Bruno, C.; Sankaran, V.; Kolla, H.; Chen, J.H. Impact of multi-component diffusion in turbulent combustion using direct numerical simulations. *Combust. Flame* **2015**, *162*, 4313–4330. [CrossRef]
32. Kee, R.J.; Coltrin, M.E.; Glarborg, P. (Eds.) *Chemically Reacting Flow: Theory and Practice*; John Wiley & Sons: Hoboken, NJ, USA, 2003; Chapter 12, pp. 528–529.
33. Van Beck, C.; Raman, V. Lagrangian-conditioned statistics of detonation propagation in a realistic rotating detonation engine. *Proc. Combust. Inst.* **2024**, *40*, 105606. [CrossRef]

34. Sharma, V.; Zhang, S.; Jain, R.; Raman, V. A mapping-based projection of detailed kinetics uncertainty onto reduced manifolds. *arXiv* **2026**, arXiv:2603.10381. [CrossRef]
35. Goodwin, D.G.; Speth, R.L.; Moffat, H.K.; Weber, B.W. Cantera: An Object-oriented Software Toolkit for Chemical Kinetics, Thermodynamics, and Transport Processes; Version 2.5.1, 2021. Available online: https://www.cantera.org (accessed on 12 March 2026).
36. Knuth, K.H. Optimal Data-Based Binning for Histograms. *arXiv* **2006**, arXiv:physics/0605197.
37. Astropy Collaboration. `astropy.stats.knuth_bin_width`: Return the Optimal Histogram Bin Width Using Knuth's Rule. Available online: https://docs.astropy.org/en/stable/api/astropy.stats.knuth_bin_width.html (accessed on 13 March 2026).
38. Pope, S.B. *Turbulent Flows*; Cambridge University Press: Cambridge, UK, 2000.

Disclaimer/Publisher's Note: The statements, opinions and data contained in all publications are solely those of the individual author(s) and contributor(s) and not of MDPI and/or the editor(s). MDPI and/or the editor(s) disclaim responsibility for any injury to people or property resulting from any ideas, methods, instructions or products referred to in the content.